



# Micro-machining of PMN-PT Crystals with Ultrashort Laser Pulses

Giovanni Piredda<sup>1</sup> · Sandra Stroj<sup>1</sup> · Dorian Ziss<sup>2</sup> · Julian Stangl<sup>2</sup> · Rinaldo Trotta<sup>3</sup> · Javier Martín-Sánchez<sup>4</sup> · Armando Rastelli<sup>2</sup>

Received: 27 November 2018 / Accepted: 29 January 2019 / Published online: 21 February 2019  
© The Author(s) 2019

## Abstract

Lead–magnesium niobate lead titanate (PMN-PT) has been proven as an excellent material for sensing and actuating applications. The fabrication of advanced ultra-small PMN-PT-based devices relies on the availability of sophisticated procedures for the micro-machining of PMN-PT thin films or bulk substrates. Approaches reported up to date include chemical etching, excimer laser ablation, and ion milling. To ensure an excellent device performance, a key mandatory feature for a micro-machining process is to preserve as far as possible the crystalline quality of the substrates; in other words, the fabrication method must induce a low density of cracks and other kind of defects. In this work, we demonstrate a relatively fast procedure for the fabrication of high-quality PMN-PT micro-machined actuators employing green femtosecond laser pulses. The fabricated devices feature the absence of extended cracks and well-defined edges with relatively low roughness, which is advantageous for the further integration of nanomaterials onto the piezoelectric actuators.

## 1 Introduction

Piezoelectric materials offer interesting properties for micro-electro-mechanical systems (MEMS) including sensing and actuating applications, as they provide wide dynamic ranges, low power consumption, and low hysteresis values [1]. Among them, lead–magnesium niobate lead titanate (PMN-PT) crystals represent an ideal material for the fabrication of actuators due to its giant piezoelectric response [2, 3]. In particular, piezoelectric actuators fabricated by femtosecond laser cutting have been recently demonstrated for tailoring the optical properties of nanomaterials [4, 5]; these

devices are based on the inverse piezoelectric effect, where the in-plane deformation state (strain) of a piezoelectric substrate upon application of an out-of-plane electric field is transferred to a medium bonded onto it. The practical implementation of such devices depends on the development of adequate procedures to machine PMN-PT thin films or substrates with strict requirements like spatial resolution within the micrometric range, sharp edges, relatively low roughness to allow fine control of small gaps between features, cleanliness to allow for subsequent bonding and metallization steps and quick fabrication to allow for repeated device development/testing cycles. The patterning of PMN-PT substrates has been performed by different means like wet etching [6], dry etching [7], reactive ion etching [8], ion milling [3, 9], and nanosecond UV laser ablation [7, 10].

The latter introduces roughening of the edges on the scale of about 10  $\mu\text{m}$  and consequently low definition in their shapes. The rest of the approaches are based on the use of lithography techniques involving the use of masks or relatively complicated processes that make the whole process slow; this is especially remarkable when relatively thick substrates (200  $\mu\text{m}$  to 300  $\mu\text{m}$ ) have to be cut through; for this kind of substrates, wet-etching processes in particular achieve limited steepness of the side walls, which in turn limits the ability to fabricate devices with small gaps of high aspect ratio. Moreover, since PMN-PT substrates are brittle, simple and maskless fabrication procedures are desirable.

✉ Giovanni Piredda  
giovanni.piredda@fhv.at

Javier Martín-Sánchez  
javiermartin@uniovi.es

<sup>1</sup> Josef Ressel Center for material processing with ultrashort pulsed lasers, Research Center for Microtechnology, Vorarlberg University of Applied Sciences, Hochschulstraße 1, 6850 Dornbirn, Austria

<sup>2</sup> Institute of Semiconductor and Solid State Physics, Johannes Kepler University, Altenbergerstraße 69, 4040 Linz, Austria

<sup>3</sup> Dipartimento di Fisica, Sapienza Università di Roma, Piazzale A. Moro 5, 00185 Roma, Italy

<sup>4</sup> Departamento de Física, Universidad de Oviedo, C/Calvo Sotelo, s/n, Oviedo 33007, Spain

Laser microfabrication with ultrashort pulses has been established in the last 10 years as a reliable technique which allows precise material ablation with very small effects on the material surrounding the ablation zone [11]. Several characteristics of ultrashort-pulse microfabrication are relevant to the preparation of PMN-PT devices. The smoothness of cut edges will prevent crack propagation and the low angle and smoothness of cut walls will allow the preparation of devices with small gaps between features. In addition, the fabrication does not involve chemical substances, whose residuals could be too aggressive for materials used in further processing steps, and the process is flexible so that devices with complex shapes can be easily fabricated. In this work, we study the micro-machining of 300-micrometer-thick PMN-PT substrates by employing amplified laser systems providing pulses with an energy of several  $\mu\text{J}$  and pulse duration of about 380 fs at the wavelength of 520 nm. The processing parameters are optimized to obtain micro-machined PMN-PT substrates with well-defined edges and arbitrary shapes. We measure ablation rates for a range of parameters and delimit the parameter region in which no heat effects occur; we examine the formation of cracks at the cut edges and the smoothness and angle of the cut walls.

## 2 Materials and experimental setup

500 micron-thick  $\text{PMN}_{0.71} - \text{PT}_{0.29}$  crystals were purchased from TRS Technologies, State College, Pennsylvania, U.S.A (from now on referred to as TRS crystals). They were lapped down to the thickness of 300  $\mu\text{m}$  and mechanically polished. For the ablation and cutting tests, we used a femtosecond laser (Spirit<sup>®</sup>, Spectra-Physics) with a nominal pulse duration of 380 fs and a pulse repetition rate settable to either 100 kHz or 200 kHz, further adjustable with the use of an acousto-optical pulse picker. The laser was operated at its second harmonic with a wavelength of 520 nm and was focused by a 100 mm f-theta telecentric objective onto the sample surface to a spot with a 7  $\mu\text{m}$  radius (measured at  $1/e^2$  intensity). For most of the experiments presented in this article, we used the base repetition rate of 100 kHz; we performed some experiments using the 200 kHz base setting obtaining modest but reproducible differences with respect to the same experiments performed with the base setting of 100 kHz (with the laser set so as to deliver pulses with the same nominal parameters). We comment further on this aspect that may indicate a sensitive dependence of surface quality on pulse parameters, in our discussion of the experiments below. For X-ray diffraction (XRD) analysis, a PANalytical X'Pert Pro MRD diffractometer was used. The high-resolution omega-2theta line scans were performed with a hybrid monochromator in the primary beam path and a Ge[220] analyser crystal in combination with a Xenon

proportional counter in the secondary beam path. For reciprocal space mapping, the diffractometer was equipped with a 1D PIXcel detector in combination with a Soller slit in the secondary beam path. For all measurements, we used copper k-alpha radiation, 8048 eV, with a corresponding wavelength of 1.5406 Å.

## 3 Results and discussion

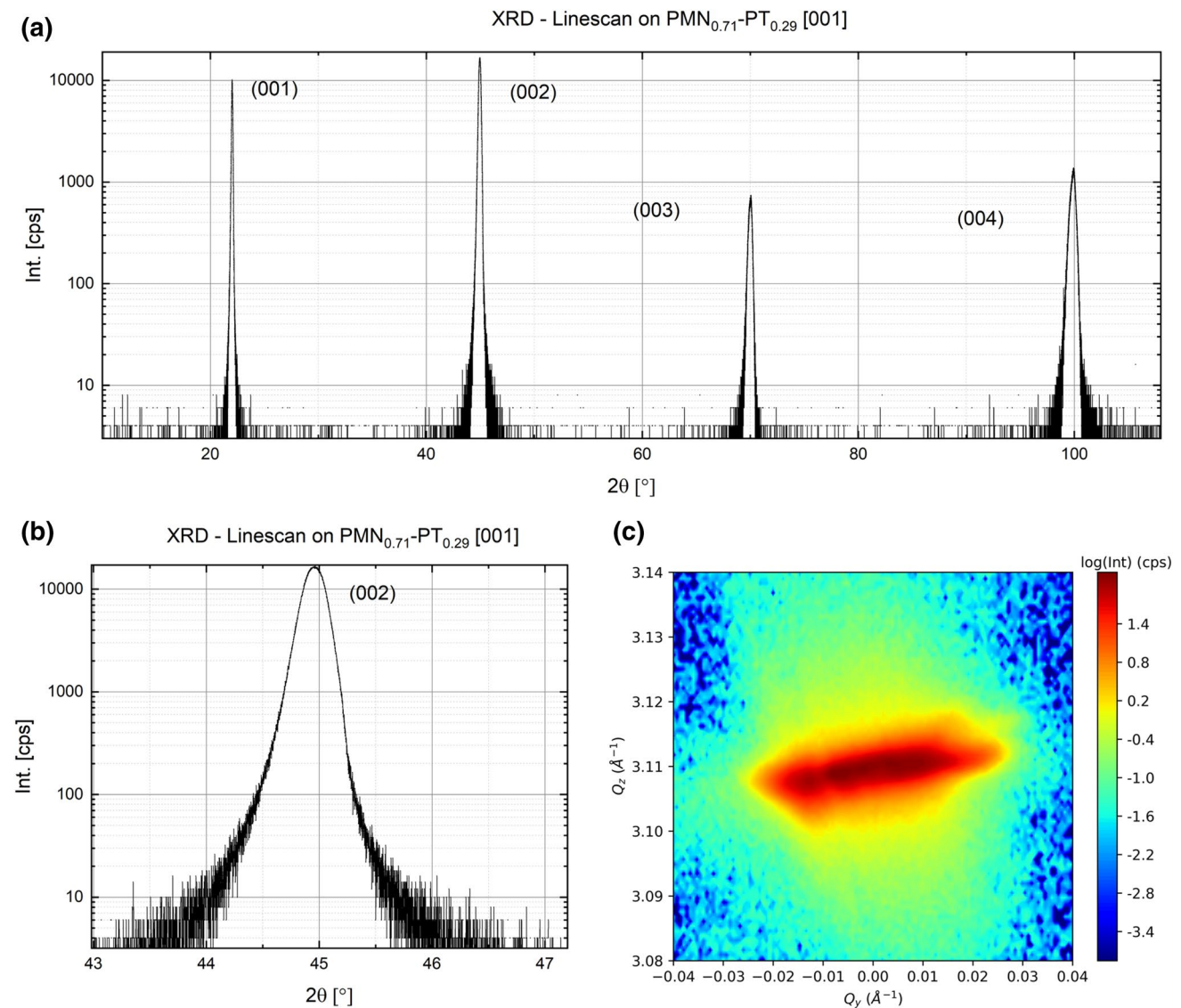
### 3.1 XRD characterization

Figure 1a shows a high-resolution omega-2theta scan performed on a single crystalline [001]-oriented PMN-PT substrate. The scan shows, as expected, a series of [00I] Bragg reflections due to the fact that this set of lattice planes is oriented parallel to the sample surface. In the zoomed-in region around the individual Bragg reflections, [panel (b) of the same figure], one can see a relatively large full-width at half-maximum (FWHM) of the individual Bragg peaks in the range of about  $0.5^\circ$  that is attributed to a more domain-like structure of the PMN-PT substrate than expected for a perfect single crystal. A reciprocal space map (RSM) around the (002) reflection is shown in panel (c) of Fig. 1, where a clear broadening of the peak along the  $Q_y$  direction indicates the presence of domains with a tilt distribution ( $\approx 0.7^\circ$ ), whereas the broadening along the  $Q_z$  direction accounts for domains with slightly different lattice parameters. These results demonstrate that the PMN-PT substrates are not perfectly single crystalline but rather a distribution of domains with different tilt angles with respect to the [001] direction. This has an impact on the mechanical stability of the substrates, since the presence of possible defects at domain boundaries can make the crystal more fragile and difficult to process. More details about the substrates used in this work can be found in [12].

### 3.2 Ablation threshold, ablation rate and heating effects

We measured the ablation threshold for the PMN-PT crystals using the method of Liu [13].

In this method, one plots the square of the radii of the ablation craters generated by laser pulses versus the logarithm of the pulse fluence; from these plots, one obtains both beam radius and ablation thresholds with a linear fit. Liu plots for single-pulse ablation of PMN-PT are shown in Fig. 2; the measured value of the ablation threshold for the TRS crystals is  $1.10 \pm 0.07 \text{ J cm}^{-2}$  when using the 100 kHz base rate setting and slightly lower,  $0.9 \pm 0.1 \text{ J cm}^{-2}$ , when using the 200 kHz base rate setting.



**Fig. 1** **a** High-resolution omega-2theta line scan of a PMN<sub>0.71</sub> – PT<sub>0.29</sub> [001] substrate; several (00l)-PMN-PT Bragg peaks can be identified in the scan. **b** Zoomed-in region around the (002) Bragg reflections scan. A broadening of the individual Bragg peaks ( $\approx 0.5^\circ$ ) indicates a domain-like structure of the measured substrate with a certain distribution of lattice spacings (with a relative variation

of the lattice constant of  $\approx 1\%$ ). **c** Reciprocal space map around the (002) reflection. The broadening in  $Q_y$  can be attributed to a tilt distribution of the individual domains with respect to the [001] crystalline direction (at  $Q_y = 0$ ) and the broadening along  $Q_z$  can again attributed to slightly different lattice parameters present in the material

This ablation threshold for PMN-PT is higher than the one found by Di Maio and co-authors for PZT ceramic for 120 fs pulses at the wavelength of 800 nm ( $0.38 \text{ J cm}^{-2}$ ) [14].

For both ablation and cutting, we move the laser beam in sequence along parallel lines (see Fig. 3); in the following, we will refer to the distance at which subsequent pulses hit the surface of the material as “pulse spacing” and to the separation between parallel lines as “line spacing”.

The ablation rate per unit energy varies as a function of pulse energy, pulse spacing and repetition rate. The energy dependence is due to physical processes which are especially

complicated for the case of dielectrics (see [15] and [16]); for metals, where a considerable part of the absorption of the light pulses is realized through linear processes, it has been modelled by several authors [17, 18] by simply considering that an optical pulse attenuates as it propagates inside the material and causes ablation if the fluence is larger than the ablation threshold; this model (which we call in the following “logarithmic model”) predicts that there is an energy at which the ablation is most efficient and has been used for the modelling of ablation of glass as well [19]. Despite its simplicity, the logarithmic model fits reasonably well

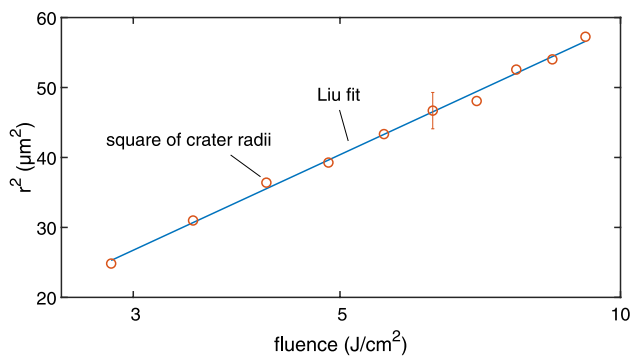


**Fig. 2** Liu plot for the TRS crystals; a representative error bar is shown on one of the experimental data points. The value of the ablation threshold resulting from the fit is  $1.10 \pm 0.07 \text{ J cm}^{-2}$ . For this plot, we used the 100 kHz base rate setting of our laser; the result with the 200 kHz base rate setting was slightly lower, equal to  $0.9 \pm 0.1 \text{ J cm}^{-2}$

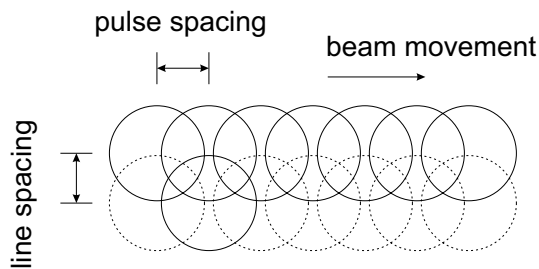


**Fig. 3** Illustration of the laser cutting procedure. Each circle represents a laser pulse incident on the sample surface; the laser beam moves in sequence along parallel lines; we refer to the distance at which subsequent pulses hit the surface of the material as “pulse spacing” and to the separation between parallel lines as “line spacing”

our experimental ablation rate for acceptable values of the parameters, as we will discuss in the next paragraphs.

The pulse spacing and repetition rate dependencies, in general terms, result from a combination of heating and incubation effects. Placing pulses closer to each other both in time and space causes the sample to heat uniformly, as each of the pulses releases some heat into the material and the dissipation is not fast enough to cool the material down before the arrival of the subsequent pulse (see, for example, the review of Finger et al. [20]); the heating of the material lowers the energy that must be deposited into it to reach evaporation and, as a consequence, lowers the ablation threshold and raises the ablation rate (see [21] for an example of ablation rate increase in metals). An estimate of the cooling time precise enough to be useful is made difficult by the lack of an estimate of the energy penetration depth at fluences below the ablation threshold; the knowledge that the cooling time is of the order of microseconds (e.g., [22]) is insufficient to predict whether the onset of heat effects will be reached at, for example, 10 or 50 kHz.

Incubation is the decrease in the ablation threshold of a material with the increase of the number of laser pulses that are applied to a given spot [23]; it can result in either an increase [24] or a decrease [25] in the ablation rate depending on the mechanism and on the values of the related changes of the physical properties of the material. We did not perform any experiment to quantify the effect of incubation in our case; however, it is sensible to expect it to be similar for all parameter sets: in our experiments, different parameter sets are not distinguished by the number of pulses per unit area, what varies is the sequence of the pulse placement.

We studied ablation as a function of the pulse energy/pulse spacing/repetition parameters in the following way. We ablated two grids of 0.5 mm-diameter circular pits using the ablation strategy illustrated in Fig. 3. In the first grid, we held the repetition rate fixed at 25 kHz and varied energy (from about 0.4 to 5.8  $\mu\text{J}$ ) and pulse spacing (from 2 to 10  $\mu\text{m}$ ), while in the second one we held the pulse spacing fixed (at 5  $\mu\text{m}$ ) and varied energy (again from about 0.4 to 5.8  $\mu\text{J}$ ) and repetition rate (from 12.5 to 100 kHz); in both cases, we set the line spacing equal to the pulse spacing, so to have the surface uniformly covered with pulses after each pass of the laser. For each pit, we chose the number of passes to reach a depth in the range 10–40  $\mu\text{m}$  (obtaining a number of passes between 3 and 60); for each pass, we chose randomly the direction of the laser beam movement.

We measured the depth of the pits using a profilometer (Dektak 8 Advanced Development Profiler); Fig. 4 shows the ablated volume (calculated from the measured pit depths) per unit energy as a function of pulse fluence. We obtained these data with the laser base repetition rate fixed at 100 kHz (and further adjusted with the help of the pulse picker). Ablation rate measurements performed on different days differed by about 10 % for pulse energies above approximately 2.5  $\mu\text{J}$ , while were reproducible to a few percent for pulse energies below this value; the variability might be due exclusively to difference in laser parameters (e.g., small differences in focusing), as different PMN-PT substrates measured on the same day gave results in good accord with each other. The larger variability at higher energies might as well be a sign of a physical effect, which we were not able to identify and might deserve further analysis. Ablation rate measurements performed with the laser base repetition rate fixed at 200 kHz (and corresponding adjustments to the pulse picker to obtain the desired repetition rates) give results consistently lower by about 30 % for pulse energies above 1  $\mu\text{J}$ , while they give similar results for lower energies. A small difference in the pulse radius between the two settings (the beam radius is of about 6.4  $\mu\text{m}$  when the laser is set at the base repetition rate of 200 kHz) is not sufficient to explain the difference using simple models, such as the linear model that we discuss in the following paragraph or a simple nonlinear absorption model.

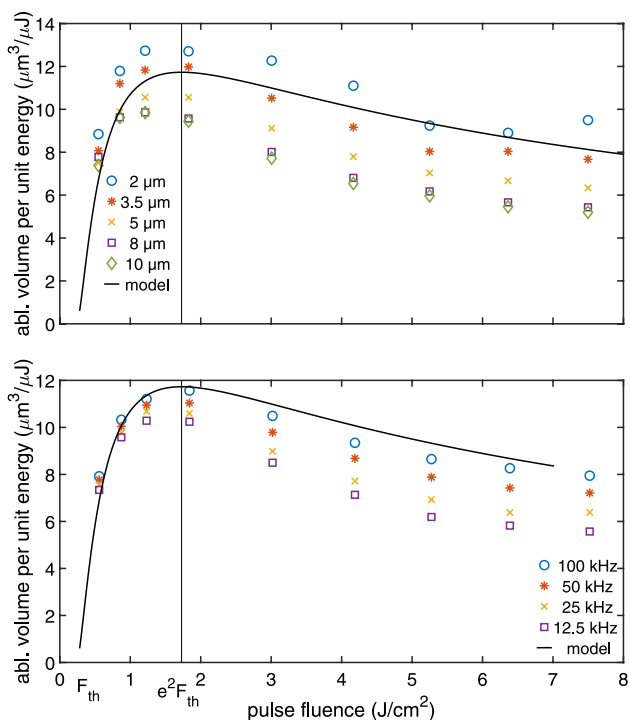


**Fig. 4** Ablation rate for PMN-PT crystals with a beam radius of 7 μm. Upper panel: pulse spacing dependence; lower panel: repetition rate dependence. Superimposed onto the experimental data is a qualitative fit to the logarithmic model for ablation; the parameters for both curves are fluence ablation threshold  $\phi_{th} = 0.24 \text{ J cm}^{-1}$  and energy penetration depth  $\delta = 0.10 \mu\text{m}$ . The threshold fluence found by the model fit is marked in the abscissa as  $F_{th}$  and the corresponding predicted optimal pulse fluence as  $e^2 F_{th}$ . The absolute error on the ablation rate is relatively large (we estimate it to around 30 %), due to the imprecise knowledge of the pulse length

We attribute then this difference to the only parameter we do not have a direct measurement of, that is the pulse duration. We add more detail about this issue in the discussion of the surface quality, where we observed as well some differences in the results obtained with the two laser settings.

Superimposed on the data, there is a qualitative fit to the logarithmic model, according to the following equation that takes into account the Gaussian profile of the laser beam [18]:

$$\Delta V_E = \frac{1}{4} \pi w_0^2 \delta \log^2 \left( \frac{\phi_0}{\phi_{th}} \right) \frac{1}{E}, \tag{1}$$

where  $\Delta V_E$  is the volume ablated per unit energy,  $w_0$  is the Gaussian beam radius,  $\delta$  is the energy penetration depth,  $\phi_0$  and  $\phi_{th}$  are the fluence at the center of the beam and the ablation threshold fluence, respectively, and  $E$  is the pulse energy; one notices the sharp increase of the ablation efficiency next to the ablation threshold, the slower decrease for high pulse energy and the highest efficiency reached for an energy of approximately  $e^2$  times the threshold for ablation. The parameters for both qualitative fits are  $\phi_{th} = 0.24 \text{ J cm}^{-1}$

and  $\delta = 0.10 \mu\text{m}$ ; the fluence threshold is lower than the one measured with the method of Liu for single-pulse ablation and the energy penetration depth results from nonlinear absorption, as PMN-PT is transparent in the visible spectrum [26]; the lower ablation threshold can be explained by the phenomenon of incubation (discussed in the preceding paragraphs). Despite the nonlinearity in the physical processes of the ablation, the simple logarithmic model fits reasonably well the shape of the curve of ablation rate versus energy using just two parameters. The character of the ablation rate curve and the presence of an optimum energy are thus at least approximately explained by the logarithmic dependence of the ablation depth on the pulse fluence and on the Gaussian beam profile; the ablation rate grows as the square of the logarithm of the pulse fluence, because both the ablation depths at points at which the fluence is above threshold and the area of the points which are above threshold grow as the logarithm of the pulse fluence.

Scanning electron micrographs of ablated surfaces are shown in Fig. 5; ablation with 2 μm and 5 μm pulse spacing result in an approximately smooth surface topography, while the topography of the surface prepared with 10 μm pulse spacing shows individual ablation craters and is for this reason rougher. The smoothness of the surfaces prepared with the 2 μm and 5 μm spacings is due to a molten layer appearing on the surface itself.

The molten layer is evident in images at high magnification (Fig. 6 is an example). The surface appearance did not prove to be completely reproducible. We observed small differences in the appearance of the molten material between different experiments (which could be due to differences in the material); in addition to this, in a group of two experiments made with the 200 kHz base repetition rate setting the molten material was not visible, and in its place flat hexagonal crystals (nanoplatelets) appear at the bottom of many of the ablated pits for all processing parameters. We show them in Fig. 7 for the case of 2 μm pulse spacing, 5.5 μJ energy, and 25 kHz laser repetition rate. The origin of this interesting phenomenon is at present unknown and may deserve further investigation also in view of the apparent sensitive dependence on laser parameters. We complete the discussion of this issue repeating the remark that the only pulse parameter of which we do not have a direct measurement is the pulse duration (nominally equal to 380 fs for all laser settings); the reason for the different duration could be in the different conversion of the infrared laser pulses (which have different energy in the two cases) in the nonlinear crystal. We hypothesize, therefore, that the differences in ablation results observed with different laser settings (and same nominal output) should be due to differences in pulse duration.

The edges of the ablated pits (shown in Fig. 8 for the 100 kHz base repetition rate setting—case of molten layer—and Fig. 9 for the 200 kHz setting—case of nanoplatelets) are

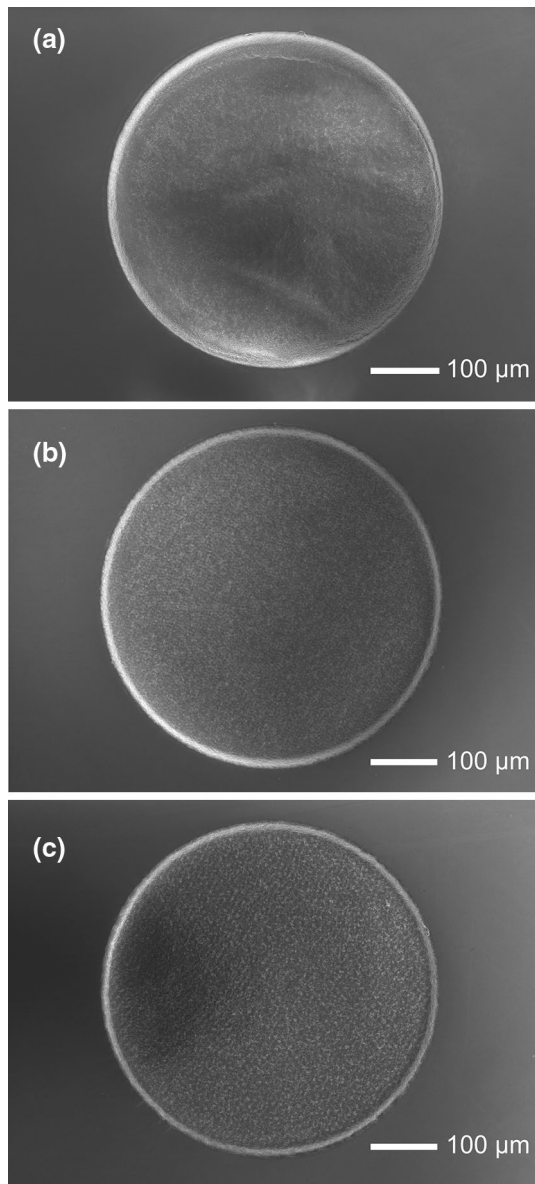


**Fig. 5** Scanning electron microscope micrograph of ablated surfaces for various ablation parameters. **a** Pulse spacing 2  $\mu\text{m}$ , energy 5.8  $\mu\text{J}$ ; **b** pulse spacing 5  $\mu\text{m}$ , energy 5.8  $\mu\text{J}$ ; **c** pulse spacing 10  $\mu\text{m}$ , energy 5.8  $\mu\text{J}$ . Repetition rate is 25 kHz for all images

generally good both for the 200 kHz and the 100 kHz base repetition rates, except for the case of base repetition rate equal to 200 kHz and pulse spacing equal to 2  $\mu\text{m}$ , where they are irregular; the jagged borders appear to result from redeposition of ablated material, although the debris might hide minor chipping (that is, separation of small fragments of materials) of the edges. A good edge quality is more difficult to achieve for cutting than for the ablation of an extended region, as cutting is performed by moving the laser in sequence along a few parallel lines; in the case of surface ablation, we arranged the path of the laser so that there is

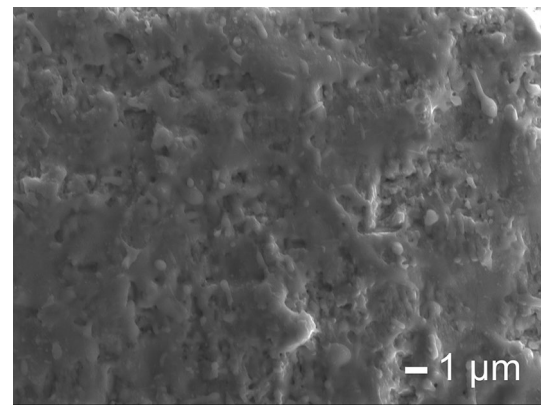


**Fig. 6** High-magnification scanning electron microscope micrograph of an ablated surfaces obtained with pulse spacing 5  $\mu\text{m}$  and energy 5.8  $\mu\text{J}$ . Repetition rate is 25 kHz. Molten material is apparent

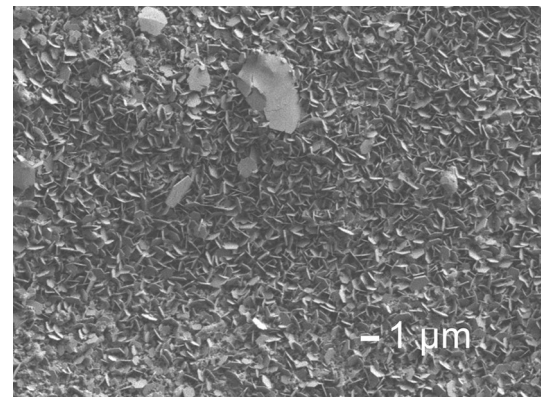


**Fig. 7** Electron microscope micrograph of pit bottom showing hexagonal crystals: pulse spacing 2  $\mu\text{m}$ , energy 5.5  $\mu\text{J}$ , and repetition rate 25 kHz

only one pulse per laser line next to the edge, so the edges have more time to cool down between subsequent pulses, while for the cuts all of the pulses are next to the edge. We examine this case more in detail in Sect. 3.3.

In conclusion, with green pulses of the duration of 380 fs and a beam radius of 7  $\mu\text{m}$  it is possible to ablate approximately  $0.4 \text{ mm}^3 \text{ min}^{-1} \text{ W}^{-1}$  of PMN-PT without heat effects and with limited redeposition of ablated material on the surface; heating starts to affect ablation strongly with pulse spacing below 5  $\mu\text{m}$  and with pulse repetition rate above 25 kHz.

### 3.3 Edge and wall quality

The cutting of crystals is realized by placing several rows of pulses next to each other (Fig. 3); repeating this procedure with a Gaussian beam results in a V-shaped groove that, when deep enough, separates two parts of the crystal. Two

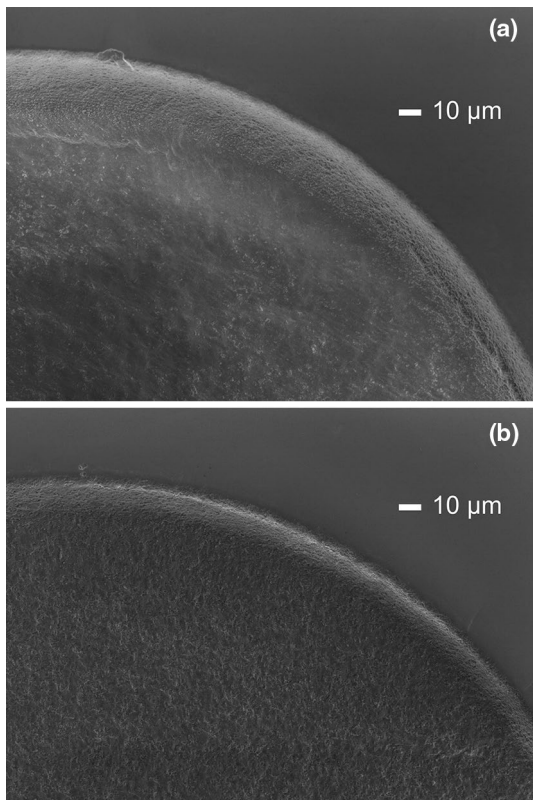


**Fig. 8** Scanning electron microscope micrograph of pit edges obtained with laser base repetition rate of 100 kHz. **a** Pulse spacing 2  $\mu\text{m}$ , energy 5.8  $\mu\text{J}$ ; **b** Pulse spacing 5  $\mu\text{m}$ , energy 5.8  $\mu\text{J}$ . Repetition rate is 25 kHz for both images

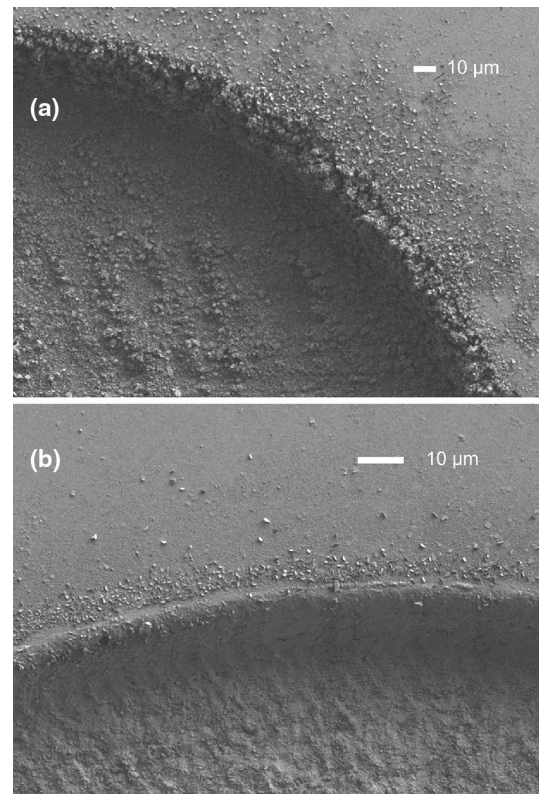


**Fig. 9** Scanning electron microscope micrograph of pit edges obtained with laser base repetition rate of 200 kHz. **a** Pulse spacing 2  $\mu\text{m}$ , energy 6.6  $\mu\text{J}$ ; **b** Pulse spacing 5  $\mu\text{m}$ , energy 6.6  $\mu\text{J}$ . Repetition rate is 25 kHz for both images

issues arise. The first issue is that cracks appear more easily than in the case of surface ablation; the second issue is that for a Gaussian beam the groove walls are inclined and become steeper as the pulse energy grows.

Cracking in the ablation with ultrashort (ps) laser pulses has been studied by Sun and co-authors for the case of glass [27]. According to their study, cracks are caused by the thermal shock of cooling; high temperatures in the case of ultrashort pulses are caused by the accumulation of energy released in the material by each of the pulses in a pulse train.

It is reasonable that in our experiments cracks should appear in cutting rather than surface ablation, since cutting and ablation are realized with different scanning strategies; in the case of cutting, one is placing several lines of pulses adjacent to each other, so that all of the pulses are close to the edge, while in the case of ablation, as illustrated in the previous section, laser scanning proceeds in random directions with respect to the edges so that usually just a few consecutive pulses are placed next to an edge. In our experiments, as we will discuss in the following paragraphs, we have seen that cracking appears at the relatively low repetition rate of 25 kHz if the pulse energy is too high. As an additional note, in the mechanism of cracking there may

be other components in addition to cooling shocks: cracks have been observed in glass after three ps pulses delivered at the frequency of 1 Hz [28] and under these conditions heat accumulation can be excluded.

A qualitative explanation for the V-shape of the groove (as, for example, discussed in [29]) is that after the first laser pass the ablation is not uniform, but is deeper at the center of the beam, where the fluence is higher; subsequent passes of the laser ablate on an inclined surface, so that the pulse fluence projected onto the surface becomes lower. Ablation stops when the projected fluence is equal to the threshold fluence, resulting in V-shaped grooves [see panel (a) of Fig. 10 for examples of grooves cut in PMN-PT crystals]; an attempt to explain quantitatively the steepening of the walls and the consequent stopping of ablation has been made by Vázquez de Aldana and coworkers for the case of fused silica including the details of propagation of the light pulses in the developing groove [30]. In the following, we refer to the stopping of ablation when the groove walls have reached a limit angle as “saturation”. A steep wall allows narrower cuts (fewer rows of pulses need to be placed alongside each other to cut through the crystal thickness), so that cutting is quicker and smaller features can be cut. Improving edge

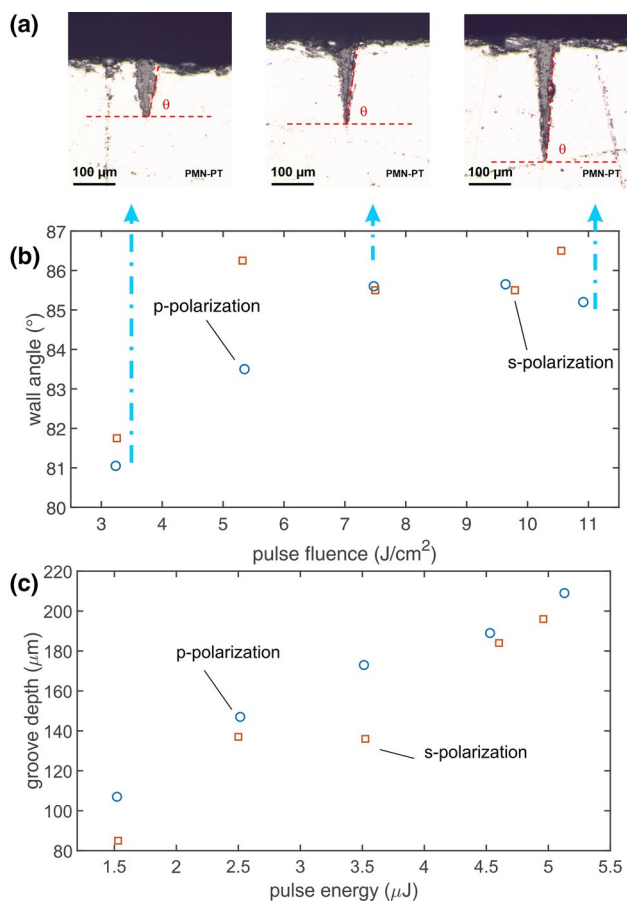


**Fig. 10** **a, b** Wall angle as a function of pulse fluence for p- and s-polarized light. **c** groove depth as a function of pulse energy for p- and s-polarized light. The grooves were cut till saturation; beam radius is 6.5 μm, pulse spacing is 5 μm and laser repetition rate is 25 kHz. The cuts are realized by placing 5 parallel lines of pulse at the distance of 5 μm from each other

quality by lowering the fluence then is achieved at expense of the wall steepness.

To investigate these issues, we carried out a cutting experiment. On a PMN-PT crystal, we placed five parallel lines of pulses, each approximately 3.5 mm long, at the distance of 5 μm from each other (as in the usual cutting procedure) and we varied the pulse energy for two different polarizations: perpendicular to the cutting lines (and so p-polarized with respect to the walls of the resulting groove) and parallel to the cutting line (and so s-polarized); the beam waist was placed at the crystal surface.

Since from our ablation experiments (Sect. 3.2), we determined that heating effects are limited for pulse spacings of 5 μm and higher and laser repetition rates of 25 kHz and smaller, we fixed 5 μm pulse spacing and 25 kHz repetition rate as processing parameters for all cutting experiments. We executed 500 passes to be sure that in all cases we cut till saturation; with five cutting lines none of the grooves cut

through the 300 μm-thick crystal, so that for each parameter set it is possible to measure the maximum cutting depth. For most of these experiments we used the 200 kHz base repetition rate setting of our laser; we used the 100 kHz base repetition rate for an examination of the quality of the full wall (see the following for details) as well as a qualitative check of edge quality, which did not result in evident differences with respect to the 200 kHz setting.

We measured the resulting cut depth, and we examined the cut edge quality both at the optical and the scanning electron microscope. For the measurement of the cut depth, we embedded the processed crystal in resin and we sectioned them, so that the measurements could be carried out with an optical microscope. For this data set and the following data set on surface cracks, the uncertainty on the knowledge of the beam radius is larger than in the case of the ablation rate experiments; this could possibly lead, in addition to a relatively high uncertainty on the cutting depths, to an overestimation of the maximum energy at which no cracks appear (an underestimation of the beam radius is more likely as an overestimation, as any imprecision in the placement of the focus can only lead to larger beam radii).

A graph of the groove depths is shown in panel (c) of Fig. 10. For a given energy, p-polarized light generates deeper cuts than s-polarized light (a known fact in general, see, for example, [31]). This can be explained with a larger absorption of p-polarized with respect to s-polarized light at the inclined walls; the price to pay is that with p-polarized light cracks and chipping form more readily than with s-polarized light. We do not possess a statistics on this very time-consuming experiment, but we can assume that the scatter of the results would be at least as high as the one observed for the ablation rates.

The angles that the groove walls form with the horizontal plane (in the following “wall angles”) are shown in panel (b) of Fig. 10 (with the accompanying panel (a) showing representative grooves) as a function of pulse fluence (the most relevant parameter for the wall angle).

A high pulse fluence leads to steeper walls for both light polarizations (advantageous, as smaller details can be cut in the piezocrystals) but too high a fluence results in chipping and cracking of the cut edges (see Figs. 11 and 13). The walls of the cut are smooth in this material next to the top (see Fig. 11). We analysed the full wall by cutting completely a 300 μm-thick substrate with pulses of 5.5 μJ energy using the repetition rate of 25 kHz and the pulse and line spacing of 5 μJ for 30 parallel lines and 500 laser passes; we placed the focus below the surface to avoid cracking (as we discuss in more detail in the following paragraphs). The resulting walls, shown in Fig. 12, are smooth with a small amount of chipping at the wall bottom.

The edge quality has a strong dependence on the polarization of the incident light. Cuts performed with s-polarized



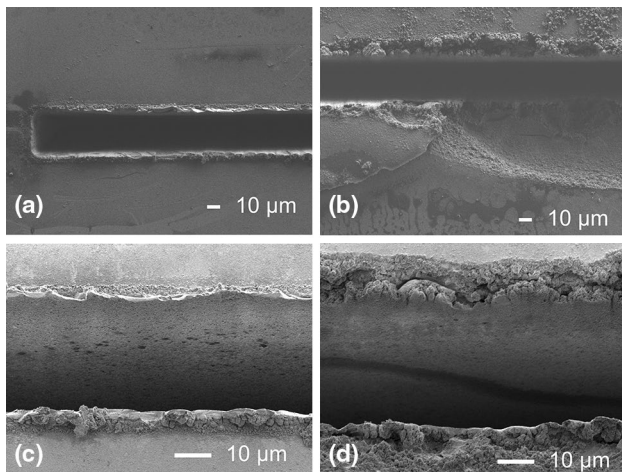


**Fig. 11** Scanning electron micrographs of cut edge (top row) and cut wall (bottom row) for cuts performed with p-polarized light. Beam radius at waist is 6.5 μm, pulse spacing is 5 μm and laser repetition rate is 25 kHz; the cuts are realized by placing 5 parallel lines of pulses at the distance of 5 μm from each other; pulse energy is 3.5 μJ (left column) and 5.7 μJ (right column); the beam waist is set at the surface. The cut edge at 5.7 μJ is cracked and chipped, while at 3.5 μJ the cracking is minimal; the cut walls are smooth in both cases

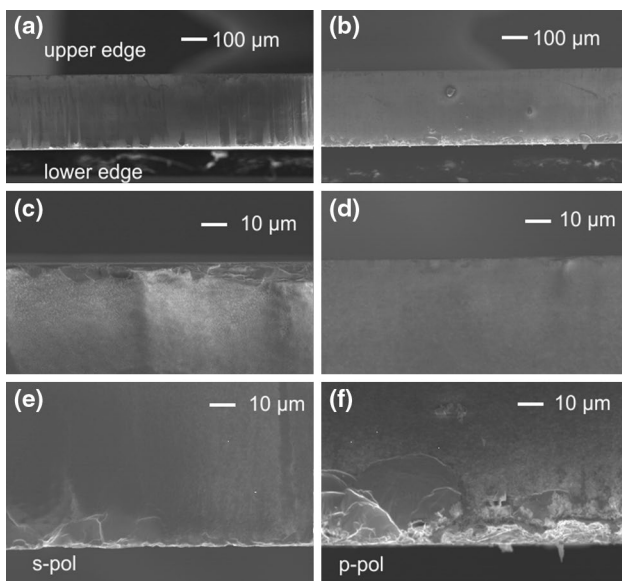


**Fig. 12** Side walls of a complete cut of a 300 μm-thick PMN-PT substrate realized with pulses of 5.5 μJ, repetition rate of 25 kHz and the pulse and line spacing of 5 μm for 30 parallel lines and 500 laser passes; the laser focus is placed in the middle of the substrate. Left column, s-polarization, right column, p-polarization; **a, b** Overview, **c, d** detail of upper edge, **e, f** detail of lower edge. The walls are smooth with a small amount of chipping at the wall bottom

light chip and crack only at the highest pulse energy which we used in the experiments (about 6.3 μJ) while cutting with p-polarized light results in cracking already at 3.5 μJ; Fig. 13

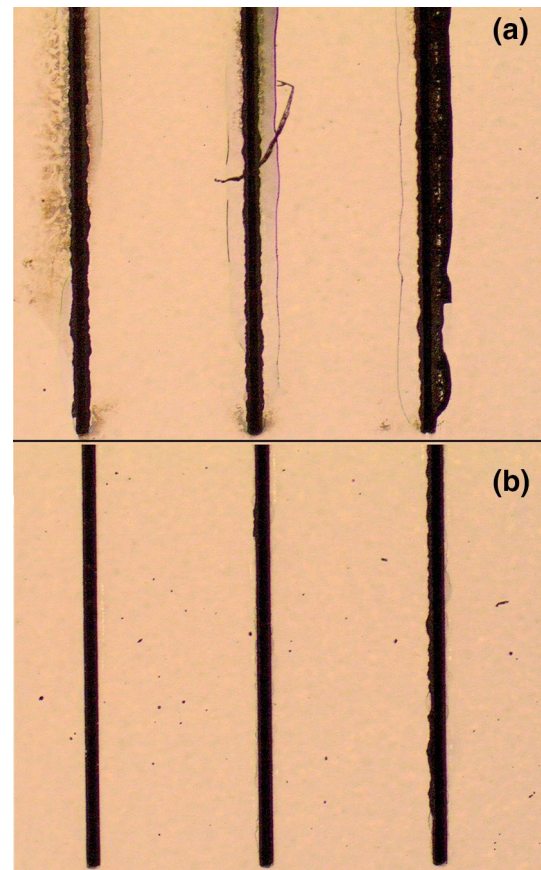
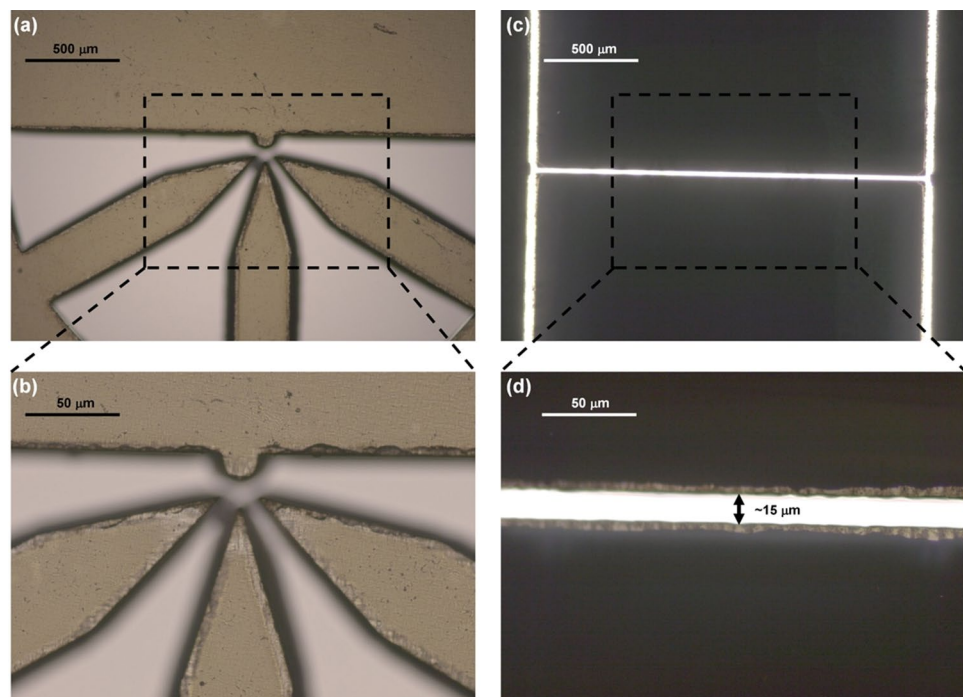


**Fig. 13** Optical microscope images of cuts performed in PMN-PT crystals under different conditions. **a** Beam waist at the surface, p-polarized light; **b** beam waist at the surface, s-polarized light. For all images, the beam radius at waist is 6.5 μm, the pulse spacing is 5 μm and the laser repetition rate is 25 kHz; the cuts are realized by placing 5 parallel lines of pulse at the distance of 5 μm from each other; pulse energy is in each panel 4.5, 5.5 and 6.3 μJ for left, middle and right cut, respectively. For s-polarized light and the energy of 6.3 μJ cracks are observed only in some of the cuts (not shown in the figure)

shows a comparison of edge quality for p- and s-polarization cutting. Combining the data on the edge quality with the data on the cut depth it would seem that cutting with s-polarized light is more convenient than cutting with p-polarized light, as it is possible to cut deeper given an acceptable edge quality; with a fixed waveplate the polarization with respect to the cut walls cannot be chosen if one is cutting a closed contour and one could attempt to cut with circularly polarized light as a compromise. In the literature several methods to tailor the light polarization, which in our case would afford more control on the quality of cuts with different orientations, have been studied; [32, 33] pursued the road of dynamically changing the polarization, while [34] experimented with circular, radial and azimuthal polarization, which are insensitive to the direction of the cut (radial and azimuthal polarizations approximate for a cutting process,

**Fig. 14** Optical images of micro-machined 300 and 200  $\mu\text{m}$  thick PMN-PT substrates. **a** Design featuring three legs with features in the micro-metric scale fabricated in a 300  $\mu\text{m}$  thick substrate. **b** Magnified picture of **(a)**, where the gaps between the fabricated legs are as small as 10  $\mu\text{m}$ . **c, d** Optical microscope images obtained in transmitted illumination of a H-shape feature, fabricated in a 200  $\mu\text{m}$  substrate, with gaps of the order of 15  $\mu\text{m}$ . Note that the size of the gaps decreases from top to bottom due to the inclination of the cut walls



respectively, p- and s-polarization states). A practical solution for a 300  $\mu\text{m}$ -thick crystal with our 7  $\mu\text{m}$  radius at the waist, that allows us to circumvent the issue of polarization, is placing the beam waist at approximately the bottom of the crystal (a precise placement is irrelevant and is made impossible by the fact that the substrates are coated with photoresist to protect the surface from the fabrication dust); in this case the quality of the edges is good up to relatively high pulse energy independently of polarization, allowing one to disregard polarization issues in practical fabrication. Using this placement of the focus we were able to use a pulse energy of 5.5  $\mu\text{J}$  and still obtain a good edge quality; as an added advantage, with this placement of the focus one avoids the readjustment of the beam focus with the progression of cutting. Note that when ablating with pulse energies sufficiently higher than the threshold small focal shifts influence just weakly the ablation rate and may even lead to its increase [35]. We summarize practical device fabrication further in Sect. 4.

In conclusion, a good compromise between processing speed and surface/edge quality is a pulse energy of 5.5  $\mu\text{J}$  with a beam waist of 7  $\mu\text{m}$ , a repetition frequency of 25 kHz and the placement of the beam waist below the surface of a thick substrate; with these parameters one is able to ablate approximately 0.06  $\text{mm}^3 \text{min}^{-1}$  of PMN-PT. With these parameters it is necessary to place the beam waist under the surface of the PMN-PT substrate to obtain crack-free edges. As a compensation for the reduced fluence at the surface, one is able to cut substrates of 300  $\mu\text{m}$  (and over) of thickness without adjustment of the beam focus.

In Fig. 14, we show optical images of 300- and 200-micrometer-thick PMN-PT substrates cut with complex shapes. These substrates were cut with the optimized conditions described in the preceding paragraph to have sharp and well-defined edges. Electrical contacts have been fabricated on both sides of the piezoelectric substrate and a voltage ramp was applied in several cycles to further check the performance of the fabricated micro-machined substrates. We did not observe any evolution of cracks and we found that the electrical response of the devices was stable. We believe that the fabrication method presented in this work opens up new possibilities for the development of advanced piezoelectric devices, where precise micro-scale feature definition is mandatory.

## 4 Conclusions

Ultrafast laser microfabrication is a flexible and rapid way to obtain devices from PMN-PT crystals. A good compromise between processing speed and surface/edge quality is a pulse energy of 5.5  $\mu\text{J}$  with a beam waist of 7  $\mu\text{m}$ , a repetition frequency of 25 kHz and the placement of the beam waist below the surface of a thick substrate; with these parameters one is able to ablate approximately 0.06  $\text{mm}^3 \text{min}^{-1}$  of PMN-PT and mm-sized devices with deep (300  $\mu\text{m}$ ) structures and gaps smaller than 50  $\mu\text{m}$  can be obtained in under 30 minutes. The fabricated devices were tested after evaporation of gold electrodes by cycling 10 times voltage ramps from 0 V to 200 V. No visible degradation (evolution of cracks) was

observed on the machined crystals after this process. Hence, such micro-machined crystals can be successfully employed for actuating applications as demonstrated in some of our recent works [4, 5, 36–38].

**Acknowledgements** Open access funding provided by FH Vorarlberg—University of Applied Sciences. The authors thank Johann Zehetner for precious indications, Thomas Auer for technical support with the sectioning of the crystals and Stephan Kasemann for electron microscope micrographs. The work was supported financially by the European Union Seventh Framework Program 209 (FP7/2007–2013) under Grant Agreement No. 601126 210 (HANAS), the AWS Austria Wirtschaftsservice, PRIZE Programme, under Grant No. P1308457, the European Research Council (ERC) under the European Unions Horizon 2020 research and innovation programme (SPQReL, Grant Agreement No. 679183), and the Christian Doppler Gesellschaft under the “Josef Ressel Zentrum für Materialbearbeitung mit ultrakurz gepulsten Laserquellen”. J.M.-S. acknowledges support from the Government of the Principality of Asturias and the European Union through a Clarín Marie Curie-COFUND grant (PA-18-ACB17-29).

**Open Access** This article is distributed under the terms of the Creative Commons Attribution 4.0 International License (<http://creativecommons.org/licenses/by/4.0/>), which permits unrestricted use, distribution, and reproduction in any medium, provided you give appropriate credit to the original author(s) and the source, provide a link to the Creative Commons license, and indicate if changes were made.

## References

1. J. Holterman, G. Pim, *Piezoelectric materials and applications* (Stichting Applied Piezo, Zaanstad, 2013)
2. S.-E. Park, T.R. Shrout, *J. Appl. Phys.* **82**(4), 1804 (1997)
3. S.-H. Baek, M.S. Rzechowski, V.A. Aksyuk, *MRS Bull.* **37**(11), 1022 (2012)
4. J. Martín-Sánchez, R. Trotta, A. Mariscal, R. Serna, G. Piredda, S. Stroj, J. Edlinger, C. Schimpf, J. Aberl, T. Lettner, J. Wildmann, H. Huang, X. Yuan, D. Ziss, J. Stangl, A. Rastelli, *Semicond. Sci. Technol.* **33**(1), 013001 (2018)
5. J. Martín-Sánchez, R. Trotta, G. Piredda, C. Schimpf, G. Trevisi, L. Seravalli, P. Frigeri, S. Stroj, T. Lettner, M. Reindl, J.S. Wildmann, J. Edlinger, A. Rastelli, *Adv. Opt. Mater.* **4**(5), 682 (2016)
6. J. Peng, C. Chao, J. Dai, H.L.W. Chan, H. Luo, *Mater. Lett.* **62**(17–18), 3127 (2008)
7. I.A. Ivan, J. Agnus, P. Lambert, *Sens. Actuators, A: Phys.* **177**, 37 (2012)
8. J. Zhang, W. Ren, X. Jing, P. Shi, X. Wu, *Ceram. Int.* **41**, S656 (2015)
9. Y. Chen, Y. Zhang, D. Karnaushenko, L. Chen, J. Hao, F. Ding, O.G. Schmidt, *Adv. Mater.* **29**(19), 1605165 (2017)
10. K.H. Lam, Y. Chen, K. Au, J. Chen, J.Y. Dai, H.S. Luo, *Mater. Res. Bull.* **48**(9), 3420 (2013)
11. K. Sugioka, M. Meunier, A. Piqué (eds.), *Laser Precision Microfabrication*, vol. 135, Springer Series in Materials Science (Springer, Berlin, 2010)
12. D. Ziss, J. Martín-Sánchez, T. Lettner, A. Halilovic, G. Trevisi, R. Trotta, A. Rastelli, J. Stangl, *J. Appl. Phys.* **121**(13), 135303 (2017)
13. J.M. Liu, *Opt. Lett.* **7**(5), 196 (1982)
14. Y. Di Maio, J.P. Colombier, P. Cazottes, E. Audouard, *Opt. Lasers Eng.* **50**(11), 1582 (2012)
15. B. Rethfeld, D.S. Ivanov, M.E. Garcia, S.I. Anisimov, *J. Phys. D: Appl. Phys.* **50**(19), 193001 (2017)
16. P. Balling, J. Schou, *Rep. Prog. Phys.* **76**(3), 036502 (2013)
17. S. Nolte, C. Momma, H. Jacobs, A. Tünnermann, B.N. Chichkov, B. Wellegehausen, H. Welling, *J. Opt. Soc. Am. B* **14**(10), 2716 (1997)
18. B. Neuenschwander, B. Jaeggi, M. Schmid, G. Hennig, *Phys. Procedia* **56**, 1047 (2014)
19. A. Ben-Yakar, R.L. Byer, *J. Appl. Phys.* **96**(9), 5316 (2004)
20. J. Finger, B. Bornschlegel, M. Reininghaus, A. Dohrn, M. Nießen, A. Gillner, R. Poprawe, *Adv. Opt. Technol.* **7**(3), 145 (2018)
21. A. Ancona, S. Döring, C. Jauregui, F. Röser, J. Limpert, S. Nolte, A. Tünnermann, *Opt. Lett.* **34**(21), 3304 (2009)
22. M. Sakakura, M. Terazima, Y. Shimotsuma, K. Miura, K. Hirao, *Opt. Express* **15**(25), 16800 (2007)
23. D. Ashkenasi, M. Lorenz, R. Stoian, A. Rosenfeld, *Appl. Surf. Sci.* **150**(1–4), 101 (1999)
24. J. Byskov-Nielsen, Short-pulse laser ablation of metals: fundamentals and applications for micro-mechanical interlocking. Ph.D. thesis, University of Aarhus (2010)
25. M. Lenzner, J. Krüger, W. Kautek, F. Krausz, *Appl. Phys. A: Mater. Sci. Process.* **69**(4), 465 (1999)
26. X. Wan, H. Luo, J. Wang, H.L.W. Chan, C.L. Choy, *Solid State Comm.* **129**(6), 401 (2004)
27. M. Sun, U. Eppelt, C. Hartmann, W. Schulz, J. Zhu, Z. Lin, *Opt. Laser Technol.* **80**, 227 (2016)
28. P.R. Herman, A. Oettl, K.P. Chen, R.S. Marjoribanks, in *Proceedings of SPIE vol 3616, Commercial and Biomedical Applications of Ultrafast Lasers*, p. 148
29. C. Fornaroli, J. Holtkamp, A. Gillner, *Phys. Procedia* **41**, 603 (2013)
30. J.R. Vázquez de Aldana, C. Méndez, L. Roso, *Opt. Express* **14**(3), 1329 (2006)
31. K. Venkatakrishnan, B. Tan, P. Stanley, N.R. Sivakumar, *J. Appl. Phys.* **92**(3), 1604 (2002)
32. Y. Jin, O.J. Allegre, W. Perrie, K. Abrams, J. Ouyang, E. Fearon, S.P. Edwardson, G. Dearden, *Opt. Express* **21**(21), 25333 (2013)
33. M. Jofre, G. Anzolin, F. Steinlechner, N. Oliverio, J.P. Torres, V. Pruneri, M.W. Mitchell, *Opt. Express* **20**(11), 12247 (2012)
34. R. Torres, T. Kaempfe, M. Delaigue, O. Parriaux, C. Hönninger, J. Lopez, R. Kling, E. Mottay, *J. Laser Micro Nanoeng.* **8**(3), 188 (2013)
35. T.-H. Chen, R. Fardel, C.B. Arnold, *Light Sci. Appl.* **7**(4), 17181 (2018)
36. R. Trotta, J. Martín-Sánchez, J.S. Wildmann, G. Piredda, M. Reindl, C. Schimpf, E. Zallo, S. Stroj, J. Edlinger, A. Rastelli, *Nat. Comm.* **7**, 10375 (2016)
37. D. Huber, M. Reindl, S.F. Covre da Silva, C. Schimpf, J. Martín-Sánchez, H. Huang, G. Piredda, J. Edlinger, A. Rastelli, R. Trotta, *Phys. Rev. Lett.* **121**(3), 033902 (2018)
38. X. Yuan, F. Weyhausen-Brinkmann, J. Martín-Sánchez, G. Piredda, V. Krápek, Y. Huo, H. Huang, C. Schimpf, O.G. Schmidt, J. Edlinger, G. Bester, R. Trotta, A. Rastelli, *Nat. Comm.* **9**(1), 3058 (2018)

**Publisher's note** Springer Nature remains neutral with regard to jurisdictional claims in published maps and institutional affiliations.